Kong, D. & Fonseca, J. *Géotechnique* [http://dx.doi.org/10.1680/jgeot.16.P.278]

Quantification of the morphology of shelly carbonate sands using 3D images

D. KONG* and J. FONSECA†

Shelly carbonate sands proliferate in regions of the world where construction of offshore structures is in high demand. These structurally weak sands have high intra-granular voids and complex angular grain shapes. To improve the understanding of the mechanical properties of the material, a detailed morphological quantification is required. This paper presents a three-dimensional characterisation of the morphology of shelly carbonate sands based on analyses of X-ray computed tomography images. Two sands from the Persian Gulf with distinct grading were investigated. An adaptive watershed segmentation technique was developed to identify the individual grains for subsequent grain-scale analysis, which overcomes the challenges posed by the intricate microstructure of these sands. Non-invasive measurements of size, intra-granular void and various shape parameters were carried out, and statistical analyses were conducted, to characterise the grains. The results help to better understand the mechanisms of grain interlocking, and the role of grain angularity and intra-granular void ratio on the mechanical behaviour of shelly carbonate sands.

KEYWORDS: calcareous soils; fabric/structure of soils; offshore engineering; particle-scale behaviour; sands

INTRODUCTION

Shelly carbonate sands are widely spread throughout the world's seabed where offshore structures such as pipelines and platforms are founded. These sands comprise the remains of marine organisms such as shells and skeletal materials, which are usually thin-walled bodies with internal voids and highly angular shapes (Semple, 1988; Golightly, 1989). Owing to the interlocking of the angular grains and the high intra-granular voids, shelly carbonate sands tend to form a very loose fabric – that is, void ratio values higher than one have been reported (e.g. Coop, 1990). The complex microstructure of these soils leads to the fact that their mechanical response is poorly understood and they have been classified as 'problematic soils' in most design guides (e.g. Jardine *et al*., 2005; API, 2007). The recent increase in offshore activity in the regions where shelly carbonate sands proliferate calls for a more scientific quantification of the grain properties of these sands.

The high compressibility has been identified as one of the most important factors affecting the mechanical behaviour of shelly carbonate sands (e.g. Yasufuku & Hyde, 1995), and the intra-granular void ratio and the collapsible nature of the material fabric are believed to contribute to the this feature (Golightly (1989) and references therein). Although soil fabric evolution into a more compacted packing is usually achieved through grain slippage and rotation, in the case of angular shelly grains, such rearrangement is likely to require prior grain damage as a means of 'unlocking mechanism'.

Shelly carbonate sands differ from more commonly investigated silica sands in many ways. One important distinction arises from composition; carbonate soils are rich in calcium carbonate, which has much lower hardness than that of quartz. The most notable characteristics of the material are, however, the high intra-granular voids and the irregular grain shapes.

The influence of grain shapes on the macro mechanical response of sands derives from the inter-granular stress transmission mechanisms (Zuriguel *et al*., 2007; Fonseca *et al*., 2016). The non-convexities and angularities of shelly grains tend to promote 'interlocking', which reduces the degrees of freedom at the contacts (Frossard, 1979) and prevents the grains from slippage (Santamarina & Cho, 2004). Shelly carbonate sands tend to form very loose internal structures, with fewer inter-granular contacts than other sands (Semple, 1988). Thus, higher inter-granular stresses are likely to be mobilised even when the sands are under relatively low loads. The influence of grain shapes on the topology of grain contacts was also reported to affect the intra-granular stress transmission and grain damage (Fonseca *et al*., 2013). In other words, point contacts are more prone to lead to crack initiation when compared to extended contact. In addition, the effect of shape on the tensile capacity of shelly grains is discussed in Nadimi & Fonseca (2017).

The understanding of the grain scale characteristics of sands has improved significantly in the last two decades using imaging techniques (e.g. Alshibli & Alsaleh, 2004; Altuhafi & Coop, 2011; Miao & Airey, 2013; Zhang & Baudet, 2013; Yan & Shi, 2014; Paniagua *et al*., 2015); in particular, the advances in high-resolution three-dimensional (3D) X-ray micro computed tomography (μCT) has contributed some extraordinary insights. This is a non-destructive technique that enables the internal structure of sands to be examined at a high level of detail. A crucial step for extracting the relevant grain scale measurements from a 3D image is to identify the individual grains through image segmentation. Given the technical challenges associated with the segmentation of grains with complex shapes and high void ratios, most of our knowledge of the shape of carbonate sands comes from

Manuscript received 1 November 2016; revised manuscript accepted 9 June 2017.
Discussion on this paper is welcomed by the editor.
* Department of Civil Engineering, City, University of London, London, UK (Orcid:0000-0002-9122-9294).
† Department of Civil Engineering, City, University of London, London, UK (Orcid:0000-0002-7654-6005).

two-dimensional (2D) analyses of thin sections or scanning electron microscopy of isolated grains (e.g. Golightly, 1989; Bowman *et al.*, 2001). However, the measurements of the shape indices based on 2D projection of a 3D grain depend greatly on the choice of the observing direction. This results in non-unique shape descriptors for a given grain, and significant differences between 2D and 3D shape indices have been previously reported (e.g. Fonseca *et al.*, 2012; Alshibli *et al.*, 2015).

This paper presents for the first time in the literature a systematic and comprehensive 3D quantification of the morphology, including size and shape, and intra-granular void ratios of shelly carbonate sands. An adaptive watershed segmentation method is developed to segment the highly irregular grains from μCT images. Subsequently, the measurements of various grain shape parameters are presented and critically discussed in the context of previous experimental measurements. Both the segmentation of the images and the analyses of the grain properties were performed using Matlab (Mathworks, 2016).

SOIL DESCRIPTION AND IMAGE ACQUISITION

Two uncemented shelly carbonate sands from the Persian Gulf are investigated. The sands have distinct grading. The coarse carbonate sand (CCS) has a median grain size, d_{50}, of 2100 μm and the fine carbonate sand (FCS) has a d_{50} of 400 μm. The mechanical behaviour of FCS has been previously documented (e.g. Wils *et al.*, 2015).

The 3D images of both sands were obtained from high-resolution μCT scans using a nanotom m (phoenix|X-ray, GE). The spatial resolution of the images is 6·67 μm and other scanning parameters include a voltage of 100 kV and a current of 280 μA. During an X-ray scanning, the objects within the sample attenuate different levels of X-ray beam energy, depending on the material composition and density. Denser materials attenuate more than less dense materials and this difference in attenuation is represented by the intensity values of the voxels (3D pixels). The contrast of intensity level allows for differentiation of the features within the image. The scanned images have the dimensions of $1050 \times 1050 \times 1050$ voxels and $2100 \times 2100 \times 1200$ voxels, for CCS and FCS, respectively. The large variety of sizes and shapes and the contrasting shades defining different grains can be seen in the 2D slices shown in Fig. 1(a) for CCS and in Fig. 1(b) for FCS. For the analysis, the sizes of the images were reduced by a factor of two due to computational limitations. The binning process consisted of merging $2 \times 2 \times 2$ voxels and assigning the mean intensity value of the group to the corresponding voxel in the reduced image.

(a)

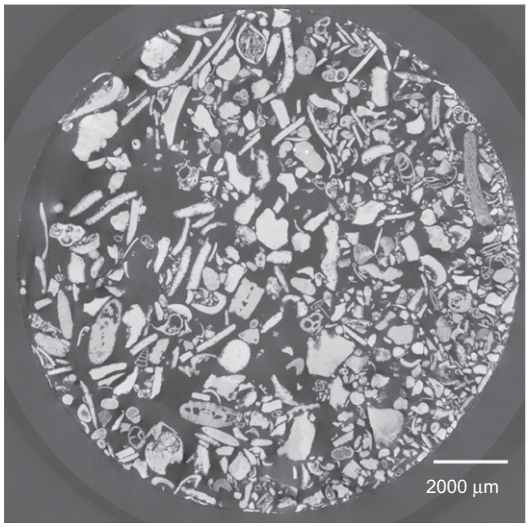

(b)

Fig. 1. Slices through 3D tomographic images of the shelly carbonate sands investigated in this study: (a) CCS; (b) FCS

IMAGE SEGMENTATION

Watershed segmentation

Image segmentation includes the processes used to identify the features of interest in the image (Gonzalez & Woods, 2008). Commonly used techniques are based on the watershed algorithm as originally proposed by Beucher & Lantuejoul (1979). For the most part, image segmentation for soil applications involves two crucial steps.

The first step is to separate the solid voxels from the void space, usually through thresholding based on Otsu's algorithm (Otsu, 1979). The outcome of the thresholding procedure is a binary image, in which solid voxels have values of 1 and void voxels have values of 0. Given the bioclastic nature of the sands, the voxels defining the solid phase, or grains, have a wide range of intensity values. For this reason, it becomes impractical to accurately group the solid voxels together using a single threshold value, as commonly used in previous studies of silica sand (e.g. Fonseca *et al.*, 2015a). Therefore, a double intensity threshold method (Henry *et al.*, 2013) was employed. Note that this step is not necessarily essential; for example, a map of gradient magnitudes of intensity values is used for segmentation by Wählby *et al.* (2004).

The second step is to segment the individual grains based on the watershed algorithm, by analogy with a geophysical model of rainfall on a terrain (Beucher & Lantuejoul, 1979). To prepare the input for the segmentation, the binary image (see the example shown in Fig. 2(a)) is converted into a 'surface' where the physical elevation is represented by a distance map (usually the inverted Euclidian distance map (IEDM)) and the individual grains are associated with a number of catchment basins (Fig. 2(b)). In this paper the basic unit that a grain is composed of in the binary image is defined as the 'element', which is a cloud of solid voxels with a convex shape (e.g. four elements can be identified in Fig. 2(a), each corresponding to a catchment basin in Figs 2(b)). The present example consists of three grains, including a two-element elongated grain (grain 1–2 corresponding to basins 1 and 2 together) in

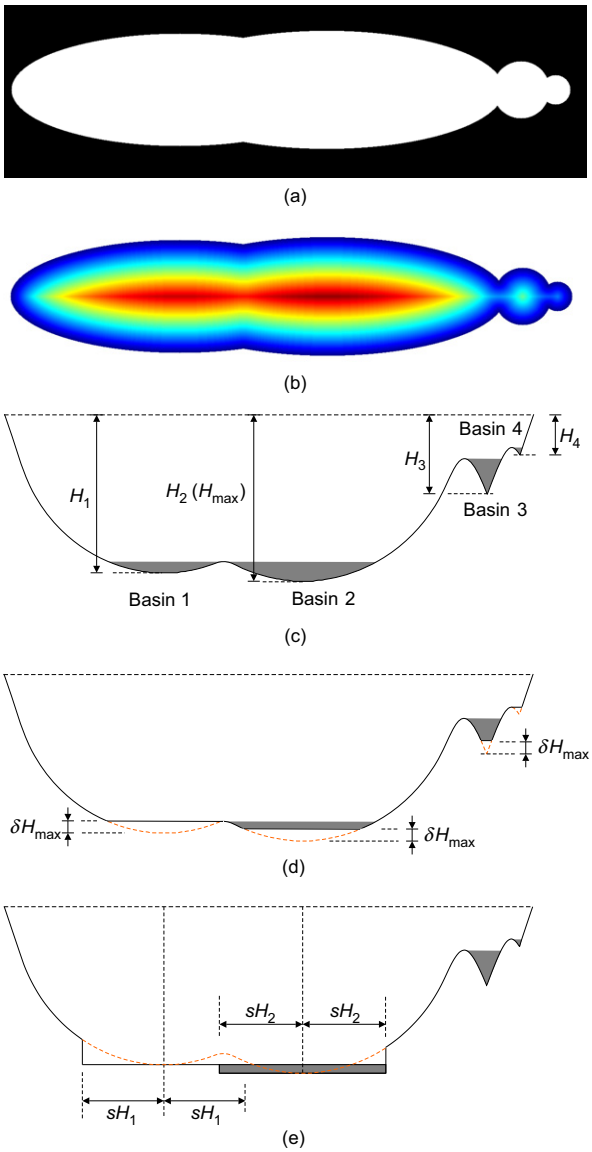

Fig. 2. Illustration of the 'bring-up' and 'bring-down' methods: (a) binary image; (b) IEDM; (c) basin profile along the central line; (d) modification of basin profile using bring-up method; (e) modification of basin profile using bring-down method (modification of basins 3 and 4 is not illustrated for clarity)

contact with two one-element grains (grains 3 and 4, corresponding to basins 3 and 4, respectively). For the sake of simplification, the elements in the present example are assumed to be symmetric and their centres are aligned. Note that the IEDM and the catchment basin profile along the central line, shown in Figs 2(b) and 2(c), respectively, are calculated results for Fig. 2(a), rather than arbitrarily drawn schematic representations.

The degree of complexity of watershed segmentation using IEDM depends on the characteristics of the grains. For example, a sample of idealised spherical grains will have point contacts throughout, and so it will be relatively easy to separate the individual grains in contact. For more realistic complex fabrics with a large variety of irregular grain shapes and contact topologies, more advanced strategies have to be developed to avoid the so-called over-segmentation problem. The essence of over-segmentation is that every element is identified as a grain, while in fact an individual grain could comprise several elements (e.g. grain 1–2 in Fig. 2(a)).

Current watershed techniques

The conventional way to alleviate over-segmentation is to fill all the catchment basins in the IEDM by an amount up to ΔH (e.g. Atwood *et al.*, 2004; Fonseca, 2011), referred to as the 'bring-up' method hereafter. The magnitude of ΔH is usually calculated as

$$\Delta H = \delta H_{\max} \tag{1}$$

where δ is the fraction factor, and $H_{\max}$ is the maximum depth of all the catchment basins (Fig. 2(c)). After the IEDM has been modified, the basins with effective depths lower than ΔH are removed, and no watershed lines will be generated. Here, the effective depth of a catchment basin is the maximum depth of water it could hold without flowing into its neighbouring basins (shaded parts in Fig. 2(c)). The drawback of this method lies in the fact that all the basins are filled by a fixed amount, and for an image with widely spanning element sizes, a reasonable value of ΔH, or δ, can hardly be found to remove the targeted basins without removing the untargeted ones. Referring to Fig. 2(d), both basins 1 and 4 are removed. Since basin 1 has greater effective depth than basin 4, it is not possible to obtain grain 1–2 while keeping grains 3 and 4 separate, which erroneously leads to two individual grains rather than three.

Recently a 'bring-down' technique was proposed by Shi & Yan (2015), which overcomes the segmentation challenges related to widely spanning element sizes. In this method, the value and location of the minima of each basin are calculated, denoted by H and X, respectively. Then, a zone measuring $(s \times H)$ from X is brought down to the same level as H, as illustrated in Fig. 2(e) for basins 1 and 2, where s is a faction factor. Since the topography is modified based on the local depth of each basin, rather than $H_{\max}$, this method is less affected by the range of element sizes. However, the effectiveness of the method is limited to the relatively bulky element shapes, which excludes the plate-like and needle-like shapes found in shelly carbonate sand. It can be observed from Fig. 2(e) that the s factor required to merge basins 1 and 2 is much higher than that to merge basins 3 and 4 (not shown for clarity), leading to the fact that over-segmentation of grain 1–2 cannot be avoided without under-segmenting (or merging) grains 3 and 4. This problem remains even if basins 3 and 4 have similar size as that of basins 1 and 2, as only the ratio of basin depth to basin range (horizontal size in the illustration) is decisive, which is determined by the element shape. Note that the elongation of the large elements is exaggerated so that the difficulty in choosing an appropriate s value for this image can be easily visualised.

A new adaptive watershed technique

In general, the limitations of the bring-up method are more related to element size, whereas those of the bring-down method are more related to element shape. To overcome these limitations, an adaptive segmentation technique is proposed here based on the bring-up method. The basic principle consists of performing a series of iterations that enable the segmentation to become progressively more refined, while largely allowing for under-segmentation in each iteration. In this method the concept of 'region' is used, which is defined as a cloud of connected solid voxels in the binary image that is not in contact with any other solid voxels. Each iteration consists of two main operations: (*a*) identifying all the regions in the binary image, and (*b*) for each region, modifying the IEDM and performing watershed segmentation accordingly.

To modify the IEDM corresponding to a region of interest, the depths of all basins are calculated and sorted

in an increasing order, that is H_1, H_2,…, H_n. Then the differences between any two adjacent values are calculated as

$$\Delta_i = H_{i+1} - H_i \quad (2)$$

If the maximum value of Δ_i can be obtained at $i = k$, then H_k is recognised as the reference depth H_0 (Fig. 3(a)). Then, all basins are filled by an amount up to $\Delta H = \delta H_0$ using the intrinsic function *imhmin*. This function suppresses all minima in the IEDM whose effective depth is less than ΔH (Fig. 3(b)). Subsequently, the basins with depths greater than $(1 - \delta)\ H_0$ are brought up to this level (Fig. 3(c)), to avoid possible over-segmentation of the grains of large size. The flow chart of the operation described here is illustrated in Fig. 4(a), where the main intrinsic functions are also given.

Under-segmentation will still take place when the watershed algorithm is applied to this modified IEDM, similar to that in the existing 'bring-up' method. However, the main focus here is to divide the initial region into a number of new regions, each with a narrower element size distribution than the initial one (see the two regions represented with distinct shades in Fig. 5(a)). These new regions will be identified in the following iteration, and watershed segmentation using the same strategy will be performed on each region. The operation is conducted iteratively until no more new regions can be identified. Each iteration is operated in a way that allows for under-segmentation (caused by the operation illustrated in Fig. 3(c)), because under-segmented grains can be segmented again in the following iterations, whereas an over-segmented grain cannot be recovered. A summary of the iterative process is shown in Fig. 4(b). All the regions in the final segmented image are recognised as individual grains (see the three regions represented with distinct shades in Fig. 5(b)) for further analysis of grain properties.

Strategy for filling the shelly grains

Another challenge related to the segmentation of shelly sands is the abundance of grains with large intra-granular voids. These grains tend to become over-segmented if not properly filled before segmentation (see Fig. 6). A filling technique using the Matlab intrinsic function *imfill* has been employed to fill all the holes in the binary image (e.g. Shi & Yan, 2015; Fonseca *et al.*, 2015b). A hole is defined as a set of void voxels that are enclosed by solid voxels (i.e. they cannot be reached by filling the background gradually from the edge of the image). Shelly grains are, however, very likely to be locally broken or naturally open, which leads to the fact that some intra-voids are not strictly enclosed and cannot be identified as 'holes'. Thus, the strategy used here consists of dividing the image into three sets of 2D slices along orthogonal directions, and then filling these slices individually using *imfill*. Subsequently, all these newly found solid voxels are superimposed on the 3D image. Using this slice-by-slice approach, most of the shelly grains can be filled, generating solid grains for the segmentation. These artificially added voxels will be removed from the image after the segmentation has been performed.

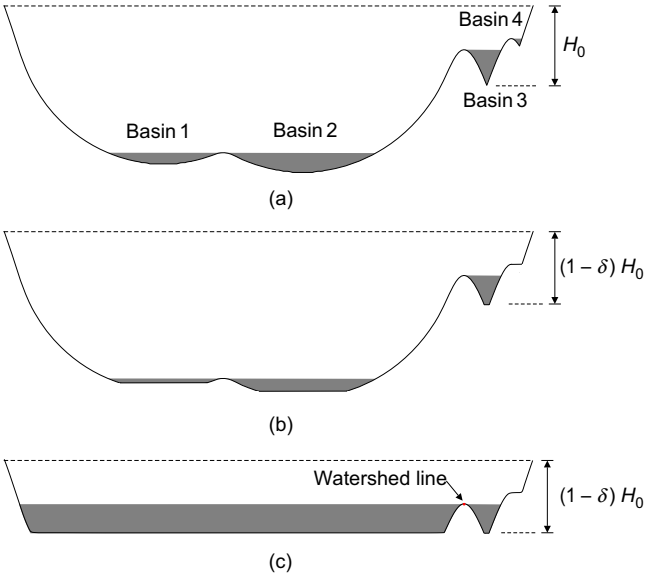

Fig. 3. Modification of catchment basin profile using the current adaptive method (one iteration is shown): (a) obtaining the referential depth H_0; (b) filling all basins by δH_0; (c) bringing up deep basins to $-(1 - \delta)H_0$

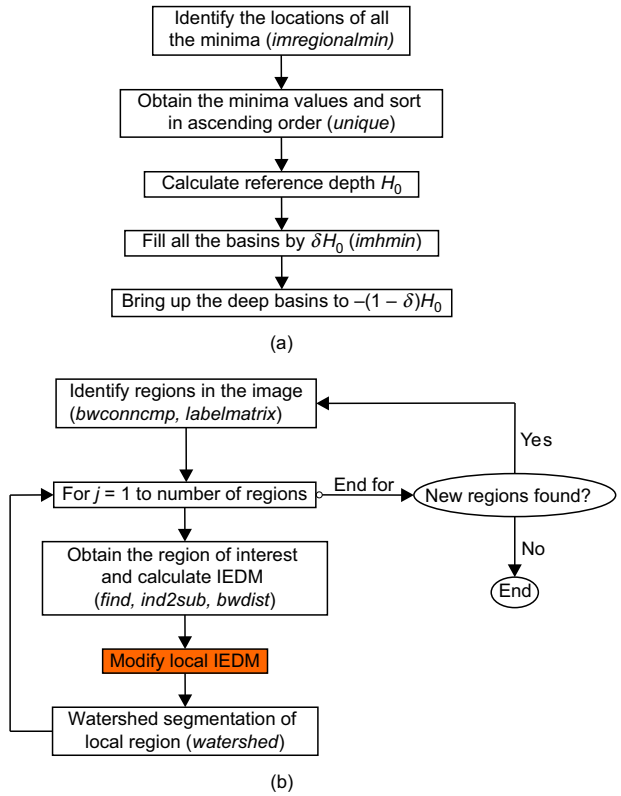

Fig. 4. Scheme of the adaptive bring-up watershed segmentation technique: (a) modification of IEDM; (b) overall process

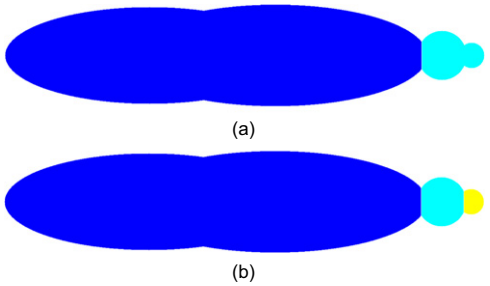

Fig. 5. Segmentation results of the example shown in Fig. 3: (a) segmented image after the first iteration; (b) segmented image after the second iteration

Fig. 6. Example showing over-segmentation caused by the high intra-granular voids using the 3D filling strategy (showing cropped part from Fig. 7(a)): (a) binary image after being filled; (b) segmented image

Segmentation results

Figures 7(a) and 8(a) show the binarisation results of the grey images in Figs 1(a) and 1(b), corresponding to CCS and FCS, respectively. It can be observed that the solid voxels are satisfactorily separated from the background for both samples, demonstrating the proper functioning of the binarisation strategy employed.

Five 2D slices from the three orthogonal directions of the 3D segmented image for CCS are presented in Fig. 7 to enable careful inspection of the segmentation results. Each slice corresponds to a row in the figure, showing 2D views of the original binary image, the binary image with filling, the segmented image with filling and the final segmented image with the artificially added voxels being removed. The final segmented image shows the very good results produced by the proposed adaptive segmentation technique, with ill-segmentation being minimised.

For FCS, three slices from different directions are presented. The segmentation process was more challenging for this sample, given the wide range of grain sizes and the abundance of needle-like and plate-like grains. The presence of these grains with irregularities or protrusions at the surface can cause severe over-segmentation, which was found to be satisfactorily alleviated by comparing the binary images with the segmented images in Fig. 8. However, these grains also tend to form extended contacts, in particular when their major axes are aligned, inevitably leading to under-segmentation. It should be noted that, for a soil sample both under-segmentation and over-segmentation could take place if watershed segmentation is performed on the original IEDM, with the under-segmentation being minimised while over-segmentation maximised. The aim of most of the improved techniques is to solve over-segmentation by modifying the IEDM and at the same time alleviate extra under-segmentation caused by this modification (e.g. Atwood *et al.*, 2004; Fonseca, 2011; Shi & Yan, 2015; Druckrey *et al.*, 2016). However, the under-segmentation resulted from the original IEDM, especially when extended contacts are present (i.e. the size of contact between two grains is greater than the short characteristic size of either grain), cannot be adequately solved within the scope of watershed segmentation methods. Overall, it can be seen that the results obtained are of good quality considering the complexity of the material.

MEASUREMENTS OF GRAIN PROPERTIES

The measurements of the grain properties comprise the intra-granular void ratio, the size and the shape parameters. The sequence of operations and algorithms employed are illustrated in Fig. 9. A total of 134 grains for CCS and 19 229 for FCS were analysed. From the segmented image, a number of regions can be identified, each denoting a grain in the soil sample. This is achieved using the intrinsic functions *bwconncomp* and *regionsprops*. Each grain is defined by a cloud of solid voxels with a common artificial intensity value, or label. For the measurement of the intra-granular void ratio, the original grains were used directly, whereas for all the other parameters, these grains were filled first. This is because only the external boundary of a grain is of importance for the quantification of size and shape. For this study, the voxels forming a grain were represented by a set of discretised points in the Cartesian coordinate system. The intrinsic function *boundary* is used to identify all the points on the external surface of the grain and generate a triangular surface mesh through Delaunay triangulation (Delaunay, 1934). This mesh is used to calculate most of the properties of the grains; for visualisation purposes and for the quantification of grain angularity, the mesh was smoothed. The aim of this mesh-smoothing step is to remove the small-scale features that will fall into roughness classification rather than overall form, according to the definitions given by Barrett (1980). The smoothing process consisted of reducing the number of triangles of a grain to a target value, in this case set to 1500, as suggested by Zhao & Wang (2016), using *reducepatch*. This function reduces the number of triangles, while preserving the overall shape of the original grain.

Intra-granular void ratio

Intra-granular void ratio (e_g) is the parameter used here to measure the enclosed voids within the grains, and is defined as follows

$$e_g = \frac{N_{void}}{N_{solid}} \tag{3}$$

where N_{solid} is the number of voxels forming the solid part of the grain and N_{void} is the number of voxel forming the enclosed voids. N_{solid} is obtained by adding the solid voxels forming the grain and N_{void} is calculated as the difference between N_{fill} and N_{solid}, where N_{fill} is the number of voxels of the grain after being filled using the slice-by-slice method previously described.

Strictly speaking, two types of enclosed voids can be found, the isolated (unconnected) voids enclosed in the grain and the enclosed voids connecting with the outer void space. Both types of voids weaken the mechanical response of the material under loading. However, the unconnected voids are more likely to contribute to the difficulties in achieving a desired B value during sample saturation, as reported in Coop (1990). Previous experimental measurements of the intra-granular porosity of carbonate sands (e.g. Golightly, 1989) suffer from the shortcoming of not being able to measure the unconnected voids. The global intra-granular void ratios for the two samples are presented in Table 1. For both samples, the unconnected intra-granular void ratio is significantly lower than the connected void ratio. Interesting to note is the fact that the e_g values for CCS are found to be more than twice those for FCS. The associated intra-granular porosities are 8·67% and 4·06% for CCS and FCS, respectively, which are within the range of 2–10% reported by Golightly (1989). Fig. 10 shows four selected grains with large intra-granular voids from CCS. The grains in Figs 10(b) and 10(c) do not have non-connected voids while those in Figs 10(a) and 10(d) have non-connected void ratio of 0·06 and 0·01, respectively.

Grain size

The grain size was quantified by means of the major, intermediate and minor axis lengths, denoted by a, b and c, respectively. These lengths were obtained using principal component analysis (PCA); more details can be found in Fonseca (2011) and Fonseca *et al.* (2012). Fig. 11 shows the cumulative distribution of the principal axes lengths of the

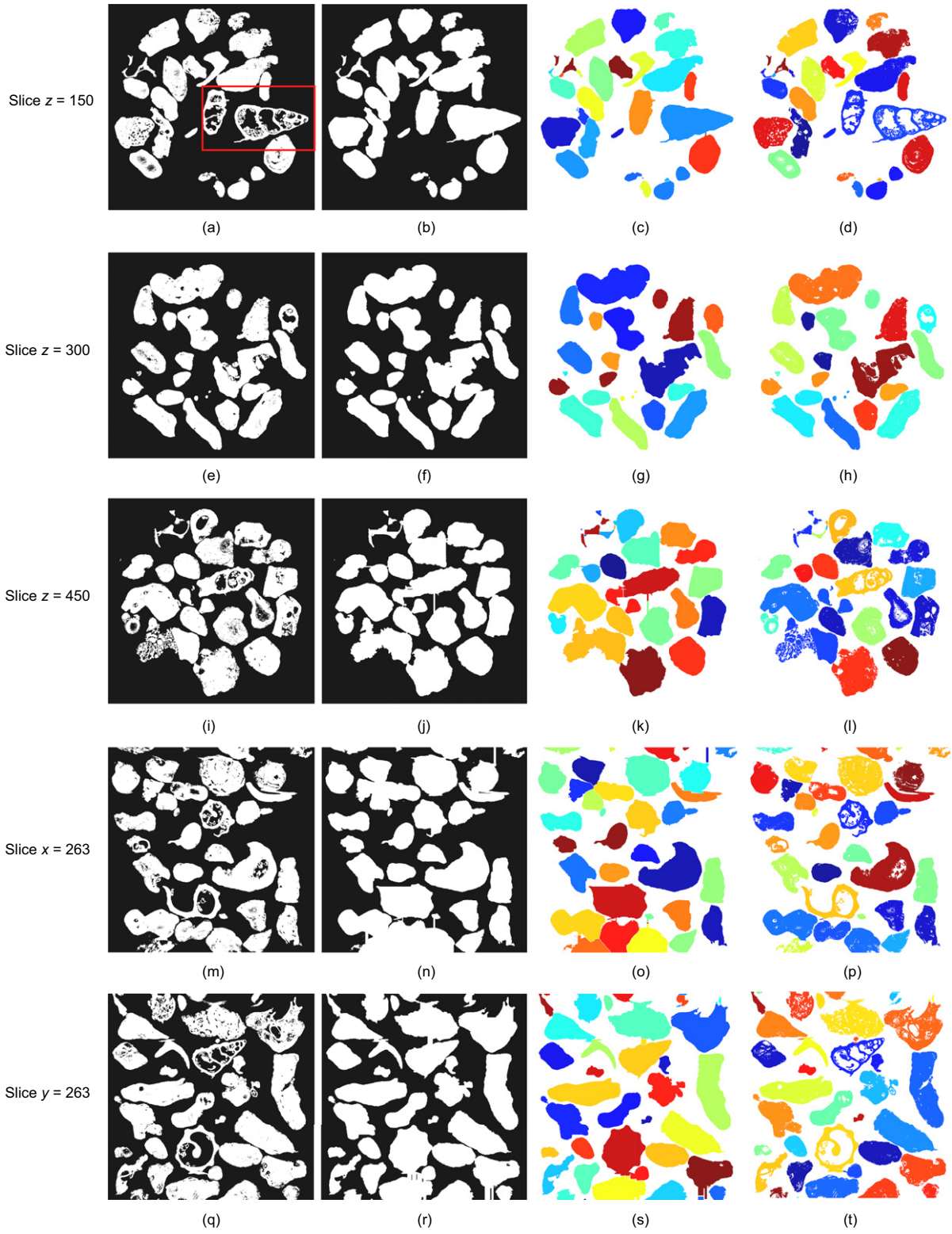

Fig. 7. Watershed segmentation results of CCS, showing 2D views of the original binary image, the binary image with filling, the segmented image with filling and the segmented image with artificially added voxels being removed (from left to right, i.e. (a) to (d); (e) to (h); (i) to (l); (m) to (p); and (q) to (t))

grains. The curves for the FCS sample are smoother when compared with CCS because of a larger number of grains. The data from the sieve analyses are also presented and compared with the image analysis results (note that for the CCS sand, the sieve analysis sample had more grains than the image used). For both samples, the sieve analysis curve lies between the curves of the intermediate and the major axes lengths, being closer to the major axis. These results are believed to be related to the abundance of platy ($a, b \gg c$) and elongated ($a, b \gg c$) grains that tend to lie with the major axis along the horizontal plane (more stable position). In this scenario, the sieve aperture should be of size greater than a for the grains to go through, unless fierce vibration is applied (which can damage the grains). Miao & Airey (2013) suggested that for carbonate sands, the experimental sieve analysis results are determined by the minor or intermediate

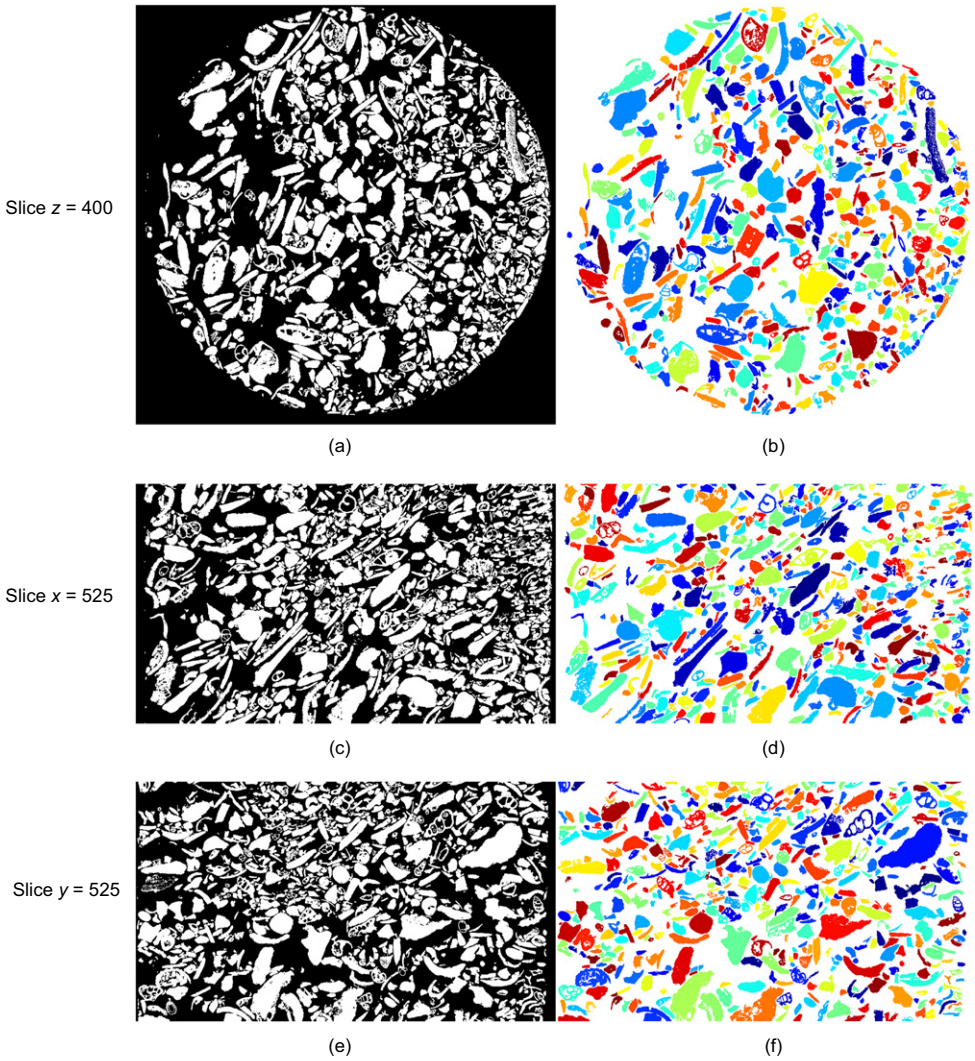

Fig. 8. Watershed segmentation results of FCS, showing 2D views of the original binary image and the segmented image (from left to right)

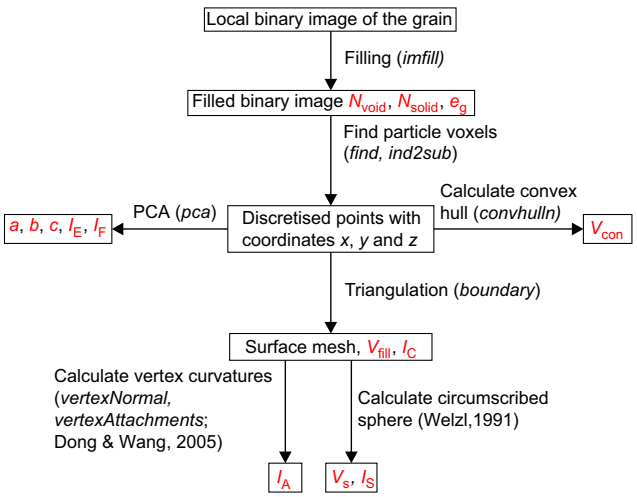

Fig. 9. Flow chart of the measurements

axes lengths, as a given grain after splitting in the major axis direction (i.e. with reduced a) is likely to fall through the same sieve aperture. For silica sand, Fonseca *et al.* (2012) showed that the sieving measurements were closer to b, while Alshibli *et al.* (2015) indicated a good agreement with a.

Table 1. Intra-granular void ratio and porosity measured for the CCS and FCS sands

	CCS	FCS
e_g	0·0949	0·0423
$e_{g(connected)}$	0·0823	0·0343
$e_{g(unconnected)}$	0·0126	0·0080
n_g	8·67%	4·06%

Shape parameters

The shape of the grains was quantified using four parameters that describe form (elongation, flatness, convexity and sphericity) and an angularity parameter that quantifies the major surface irregularities (i.e. edges and corners), as originally proposed by Barrett (1980). The rationale for the definition of these parameters was that the values should theoretically vary between zero and one, the latter corresponding to an ideal shape. This principle simplifies the understanding of the geometrical meaning of these parameters and provides a better link between visualisation and quantification.

Elongation and flatness indices. Based on the measurements of the three axes lengths, the elongation (I_E) and flatness (I_F)

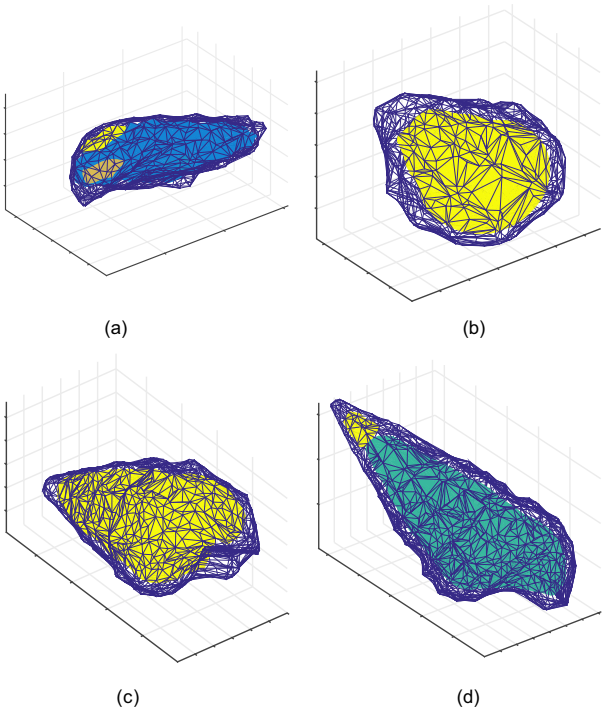

Fig. 10. Typical grains with different intra-granular void ratios: (a) $e_g = 0{\cdot}38$; (b) $e_g = 0{\cdot}57$; (c) $e_g = 0{\cdot}69$; (d) $e_g = 0{\cdot}82$

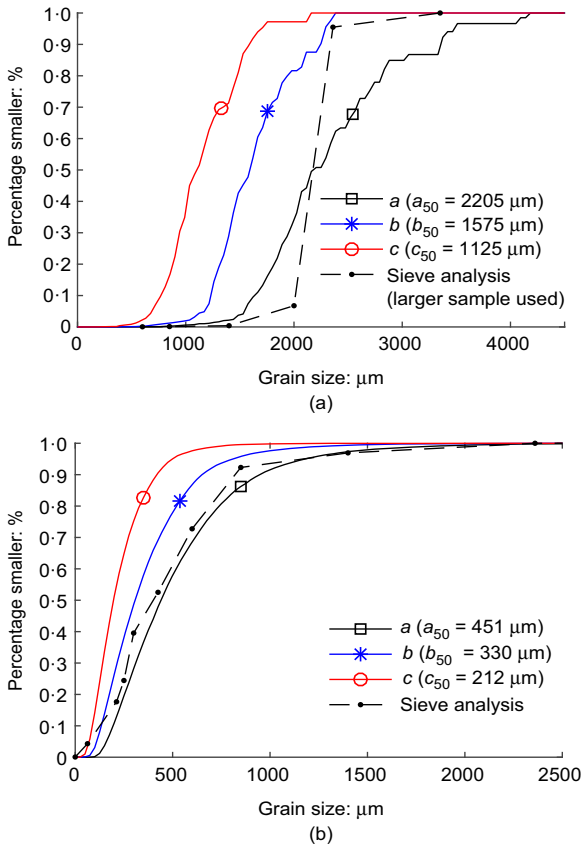

Fig. 11. Particle size distribution of the two sands: (a) CCS; (b) FCS

of a grain are, respectively, defined here as follows

$$I_E = \frac{a - b}{a} \tag{4}$$

$$I_F = \frac{b - c}{b} \tag{5}$$

The definitions of flatness and elongation here differ from those used in previous studies: b/a and c/b, for elongation and flatness, respectively (e.g. Clayton *et al.*, 2009; Fonseca *et al.*, 2012). The definitions were modified here to guarantee that the degree to which a grain is elongated or flat in shape is positively correlated to the corresponding indices (i.e. $I_E \approx 1$ for needle-like and $I_F \approx 1$ for a platy grain). Fig. 12 illustrates the ability of these indices to capture the shape of four chosen grains with typical shapes: very elongated or needle-like (Fig. 12(a)), plate-like (Fig. 12(b)) and bulky (Figs 12(c) and 12(d)). Although the shapes of the needle-like and plate-like grains are well represented by these two indices, it is clear that additional parameters are required to capture the overall shape for the bulkier grains.

Convexity index. The convexity index I_C is used in this study to evaluate how closely the grain represents a convex hull. This index is calculated as

$$I_C = \frac{V_{fill}}{V_{con}} \tag{6}$$

where V_{fill} is the volume of the grain after being filled, calculated based on the triangular surface mesh described above, and V_{con} is the volume of the minimum convex hull that encloses the grain. The convex hull was obtained using the intrinsic function *convhulln*, which generates a triangular mesh enclosing the convex surface of the grain through Delaunay triangulation. The volume enclosed by the mesh can also be obtained using this function.

Figure 13 shows the triangular surface mesh of four typical grains with various convexity values. The meshes of the convex hulls for these grains are also presented. The two grains shown in Figs 13(c) and 13(d) are the same grains, respectively, as shown in Figs 12(d) and 12(c). The grain in Fig. 12(d) (also in Fig. 13(c)) has lower I_E and I_F values than those of the grain in Fig. 12(c) (also in Fig. 13(d)), which suggests a more bulky shape for the former. However, through visual inspection and comparison of convexity values (0·71 to 0·93), this grain appears to be less bulky.

Sphericity index. As discussed by Clayton *et al.* (2009), there are various definitions for the sphericity index; the definitions available in the literature include 2D indices (e.g. Alshibli & Alsaleh, 2004; Cho *et al.*, 2006) and 3D indices (e.g. Hawkins, 1993; Fonseca *et al.*, 2012; Alshibli *et al.*, 2015). There is no real consensus on which formulation is more effective to describe sphericity. In this study, a new definition for the sphericity index (I_S) is proposed, which is calculated as

$$I_S = \frac{V_{fill}}{V_s} \tag{7}$$

where V_s is the volume of the circumscribed sphere of the grain, with radius R_o. More details of the derivation of R_o can be referred to Welzl (1991). A similar definition was adopted by Alshibli *et al.* (2015); in their definition, however, the referential sphere has a diameter equal to c, which can yield I_S values greater than one. The advantage of the definition presented here is that the maximum theoretical value for sphericity is 1 (i.e. a perfect sphere).

Two typical grains with different levels of sphericity are shown in Fig. 14. The grain presented in Fig. 14(a) is very elongated and exhibits a large deviation from a spherical shape and a sphericity value of 0·09. The grain in Fig. 14(b)

exhibits a more bulky shape with a higher sphericity value of 0·44. Using the circumscribed sphere as the referential sphere helps the sphericity index to be intuitively estimated through visualisation. As expected, increasingly elongated grains have lower values of sphericity, which was also reported by Bowman *et al.* (2001) using 2D measurements.

Angularity index. All the shape parameters introduced so far were related to form and cannot be used to capture the sharpness of the protrusions on the grain surface, such as edges and corners. A new angularity index (I_A) is introduced here to quantify major surface irregularities, so that rounded grains will yield low I_A and angular grains will have high I_A values.

Based on the triangular mesh of the grain surface, the curvature of each vertex of the mesh was estimated using the method proposed by Dong & Wang (2005). The curvature at a vertex reveals how much a local surface deviates from a flat plane (i.e. a sphere with radius R has a curvature of $1/R$ at any point of its surface). For the estimation of the curvature of a vertex on the mesh, a key step is to obtain the normal vectors to this vertex and to the other vertices connecting to it. This was achieved by using the intrinsic functions *vertexNormal* and *vertexAttachments*. More details on how to obtain the curvature based on these variables can be found in Dong & Wang (2005). The outputs of this calculation are the maximum and minimum principal curvatures, k_1 and k_2, of the vertices. In the 3D space, a positive value of curvature indicates that the surface is locally convex and a negative value indicates otherwise.

The mean curvature, taken as the average of k_1 and k_2, was reported to be adequate to capture the curvature of a vertex on the 3D surface mesh for silica sand grains (Zhao & Wang, 2016). For the case of shelly carbonate grains, the highly irregular and concave shapes lead to negative k_2 values, and for this reason k_m was obtained by averaging the absolute values of k_1 and k_2. Since the curvature has the dimension of m^{-1}, k_m was normalised by a referential curvature defined here as $k_{in} = 1/R_{in}$, where R_{in} is the radius of the inscribed sphere of the grain. For an individual grain, the vertices with k_m/k_{in} greater than one are identified as having high curvatures. Based on the k_m values of the vertices on the mesh, a parameter I_A is proposed here as follows

$$I_A = \frac{\sum \{A_j \times \max[0, \text{sign}(k_{m,j} - k_{in})]\}}{\sum A_j} \quad (8)$$

where A_j and $k_{m,j}$ are the area and the mean curvature of the jth triangle in the mesh, respectively. The mean curvature of a given triangle was obtained by averaging the values of its three vertices. This parameter provides an indication of the proportion of the grain surface that is associated with sharp corners. Fig. 15 shows an example of an extremely angular shape ($I_A = 1$).

Figure 16 shows the distribution of the normalised curvature k_m/k_{in} on the grain surfaces for six selected grains. The surface of each grain is shaded according to the local curvature values and the sharper corners are associated with lighter shades. As expected, the grains in Fig. 16 with more sharp corners (and thus light shades) exhibit higher

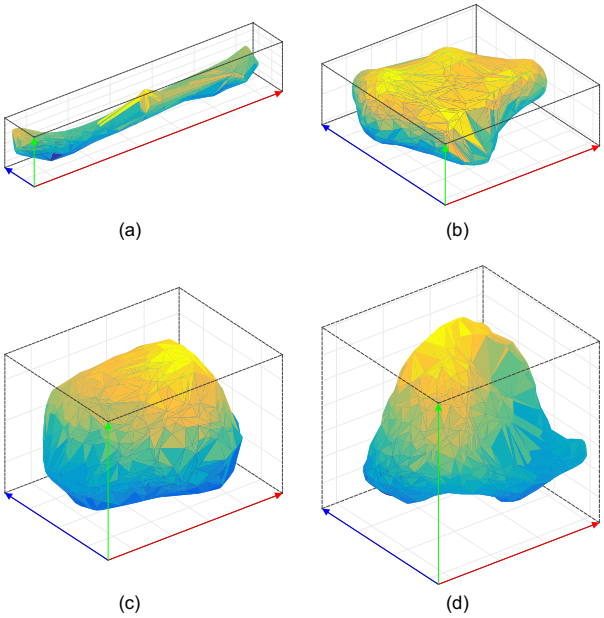

Fig. 12. Typical grains with different elongation and flatness values: (a) $I_E = 0{\cdot}82$, $I_F = 0{\cdot}16$; (b) $I_E = 0{\cdot}04$, $I_F = 0{\cdot}64$; (c) $I_E = 0{\cdot}23$, $I_F = 0{\cdot}06$; (d) $I_E = 0{\cdot}03$, $I_F = 0{\cdot}05$

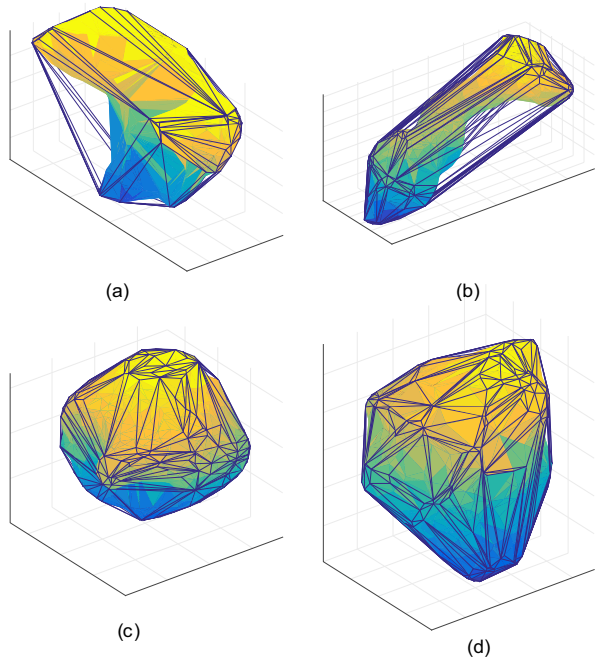

Fig. 13. Typical grains with different convexity values: (a) $I_C = 0{\cdot}42$; (b) $I_C = 0{\cdot}52$; (c) $I_C = 0{\cdot}71$; (d) $I_C = 0{\cdot}93$

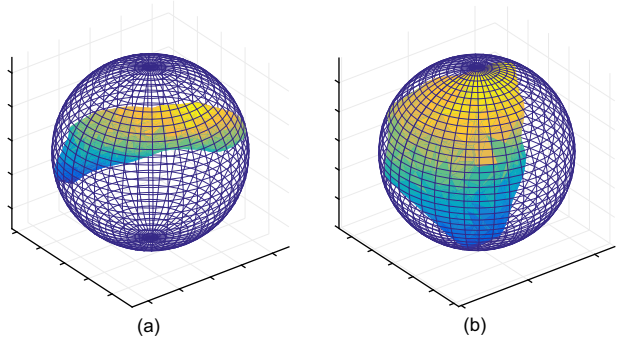

Fig. 14. Typical grains with different sphericity values: (a) $I_S = 0{\cdot}09$; (b) $I_S = 0{\cdot}44$

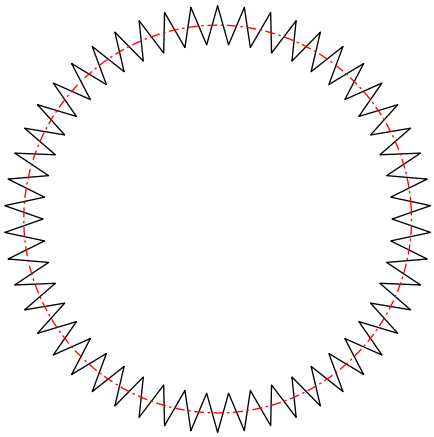

Fig. 15. Two-dimensional projection of an artificial grain with $I_A = 1$

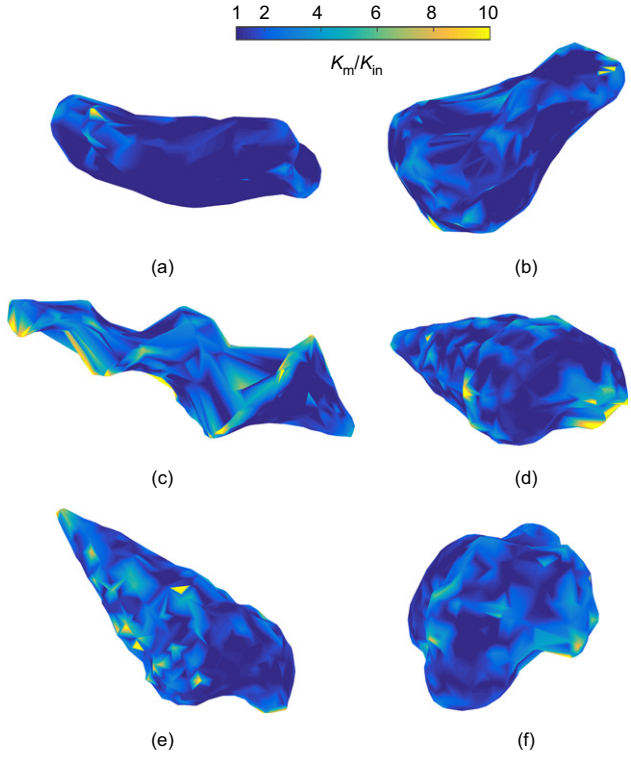

Fig. 16. Typical grains with various angularity values: (a) $I_A = 0{\cdot}03$; (b) $I_A = 0{\cdot}15$; (c) $I_A = 0{\cdot}21$; (d) $I_A = 0{\cdot}27$; (e) $I_A = 0{\cdot}41$; (f) $I_A = 0{\cdot}51$

angularity values, indicating the effectiveness of using the proposed parameter I_A to measure angularity.

Statistical analysis and correlations

The cumulative distributions of the shape parameters introduced above are presented in Figs 17(a) and 17(b) for CCS and FCS, respectively. Despite the different grading of the two samples, similar distribution patterns can be observed. The median values of flatness (I_{F50}), elongation (I_{E50}), convexity (I_{C50}) and sphericity (I_{S50}) for the two sands are also shown to be very similar. The angularity distribution is slightly distinct, with I_{A50} values of 0·13 and 0·08 for CCS and FCS, respectively. This higher angularity of CCS was confirmed by visual inspection of the grains. The parameter taking higher values is convexity, and it can be seen that

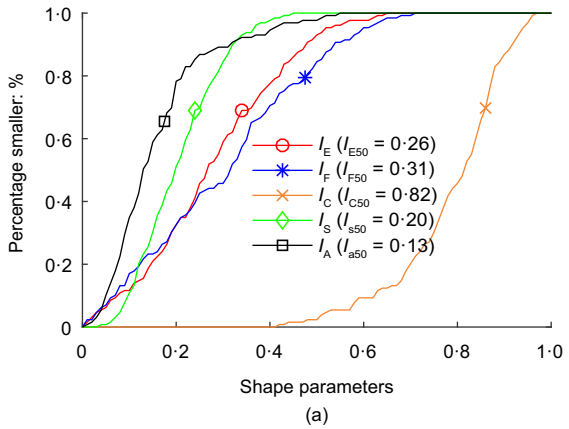

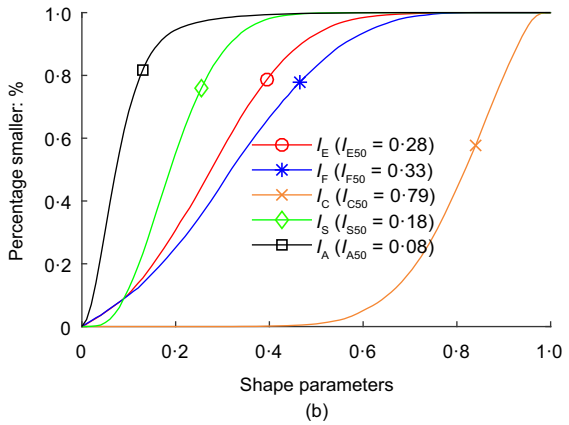

Fig. 17. Cumulative distributions of shape parameters: (a) CCS; (b) FCS

almost half of the grains have I_C above 0·8, for both sands. The distribution curves for elongation and flatness are relatively close, with ultimate values slightly lower than 0·8. Almost all grains are found to have sphericity values below 0·5, which is a good indicator of the irregularity of grains forming this bioclastic sand.

Figures 18(a) and 18(b) show the correlation between convexity and sphericity. In general, a clear linear upper bound can be observed, indicating that high sphericity values can only be achieved for grains with high convexivity. In other words, concavities in the grains significantly reduce the measured sphericity value. This strong correlation has also been observed in previous studies of silica grains (Fonseca *et al.*, 2012).

Figures 18(c) and 18(d) show the correlation between elongation and sphericity, where linear lower and upper bounds can be clearly observed, exhibiting a decreasing trend. High I_S values can only be observed for grains with low I_E values. Different observations can be made for the relationship between elongation and convexity, which appears essentially uncorrelated (i.e. full range of I_C values can be measured for different I_E values).

Figures 18(e) and 18(f) show that the distribution of angularity values is uncorrelated with both convexity and sphericity. This observation confirms that the proposed angularity index provides additional information of grain shape that the form indices I_C and I_S are not able to capture. Similar observations were found for I_E and I_F against I_A (although not presented here). It is also worth mentioning that no correlation was found between shape parameters and the intra-granular void ratio. Furthermore, size was found to be independent of shape. Overall, despite the distinct difference in grading and number of grains between

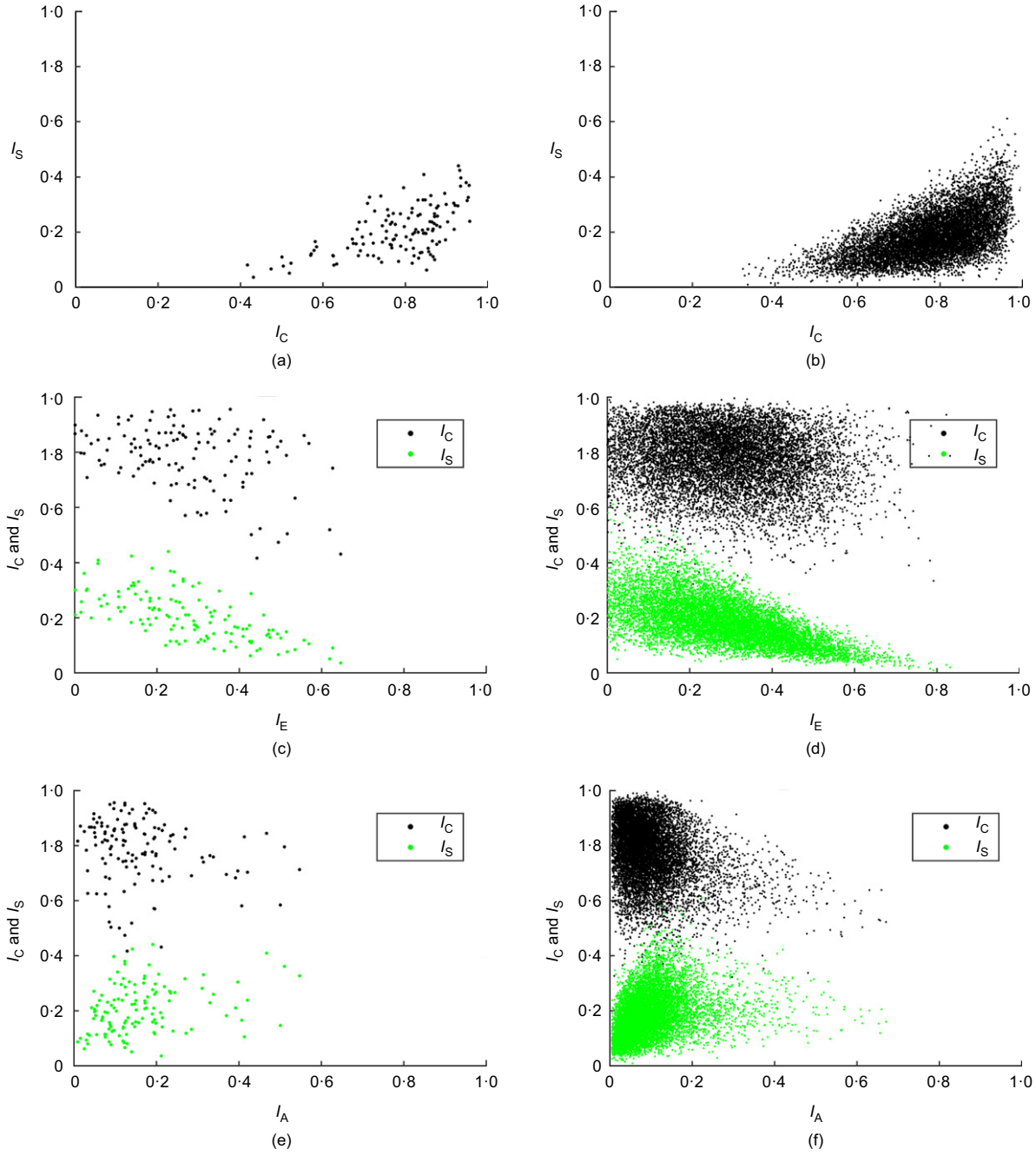

Fig. 18. Correlations between different shape parameters: (a) sphericity against convexity for CCS; (b) sphericity against convexity for FCS; (c) convexity and sphericity against elongation for CCS; (d) convexity and sphericity against elongation for CCS; (e) convexity and sphericity against angularity for CCS; (f) convexity and sphericity against angularity for FCS

CCS and FCS, very similar correlation patterns were found for both cases.

CONCLUSIONS

This paper presents a detailed quantification of the grain properties of shelly carbonate sands using 3D images obtained from X-ray computed tomography. This is a significant step towards a better understanding of the microstructure of these shelly sands, which differs considerably from more commonly studied silica sands of terrigeneous origin. An in-house Matlab code was developed to segment the images in order to extract the relevant grain-scale measurements in terms of intra-granular void ratio, size and shape. The main findings are summarised as follows.

The segmentation results show that this technique successfully overcomes major challenges posed by the large diversity and complexity of the shapes associated with the bioclastic nature of shelly sands. The key advantages of this new technique are: (*a*) its iterative nature that enables an image to become progressively segmented, and (*b*) the use of truly adaptive parameters that are determined at the local rather than global level. Given the ability of the technique to deal with extreme grain morphologies, it can be readily used to segment other granular materials.

The shape parameters proposed here are shown to capture well the variety of grain shapes and to provide more intuitive and meaningful metrics. In particular, the newly proposed angularity parameter based on grain surface curvatures was found to provide a good description of the corners and sharp

edges of shelly grains. The image-based approach used here enables more accurate measurements of intra-granular void ratio and grain size distribution, when compared with invasive experimental methods.

ACKNOWLEDGEMENTS

The authors would like to thank the Engineering and Physical Sciences Research Council (EPSRC) for their financial support (EP/N018168/1) and acknowledge Mr Gerhard Zacher from GE Sensing & Inspection Technologies GmbH (Germany) for his help in the acquisition of the tomographic images.

NOTATION

a, b, c	major, intermediate and minor principal axes lengths
d_{50}	median grain size
e_g	intra-granular void ratio
H_{max}	maximum depth of catchment basins in region of interest
H_0	referential depth of catchment basins in region of interest
I_A	angularity index
I_C	convexity index
I_E	elongation index
I_F	flatness index
I_S	sphericity index
N_{fill}	total number of voxels of the grain after being filled
N_{solid}	total number of solid voxels of the grain
N_{void}	total number of void voxels of the grain
n_g	intra-granular porosity
R_{in}	radius of inscribed sphere
R_o	radius of circumscribed sphere
s	faction factor used in the bring-down method
V_{con}	volume of minimum convex hull
V_{fill}	volume of grain after being filled
V_s	volume of circumscribed sphere
δ	faction factor used in the bring-up method

REFERENCES

Alshibli, K. & Alsaleh, M. (2004). Characterizing surface roughness and shape of sands using digital microscopy. *J. Comput. Civ. Engng* **18**, No. 1, 36–45.

Alshibli, K., Druckrey, A., Al-Raoush, R., Weiskittel, T. & Lavrik, N. (2015). Quantifying morphology of sands using 3D imaging. *J. Mater. Civ. Engng* **27**, No. 10, https://doi.org/10.1061/(ASCE)MT.1943-5533.0001246.

Altuhafi, F. N. & Coop, M. R. (2011). Changes to particle characteristics associated with the compression of sands. *Géotechnique* **61**, No. 6, 459–471, http://dx.doi.org/10.1680/geot.9.P.114.

API (American Petroleum Institute) (2007). *Recommended practice for offshore platforms*. Washington, DC, USA: API.

Atwood, R. C., Jones, J. R., Lee, P. D. & Hench, L. L. (2004). Analysis of pore interconnectivity in bioactive glass foams using X-ray microtomography. *Scripta Mater.* **51**, No. 11, 1029–1033.

Barrett, P. J. (1980). The shape of rock particles, a critical review. *Sedimentology* **27**, No. 3, 291–303.

Beucher, S. & Lantuejoul, C. (1979). Use of watersheds in contour detection. *Proceedings of international workshop on image processing: real-time edge and motion detection/estimation*, Rennes, France, pp. 17–21.

Bowman, E. T., Soga, K. & Drummon, W. (2001). Particle shape characterisation using Fourier descriptor analysis. *Géotechnique* **51**, No. 6, 545–554, http://dx.doi.org/10.1680/geot.2001.51.6.545.

Cho, G. C., Dodds, J. & Santamarina, J. C. (2006). Particle shape effects on packing density, stiffness and strength: natural and crushed sands. *J. Geotech. Geoenviron. Engng* **132**, No. 5, 591–602.

Clayton, C. R. I., Abbireddy, C. O. R. & Schiebel, R. (2009). A method of estimating the form of coarse particulates. *Géotechnique* **59**, No. 6, 493–501, http://dx.doi.org/10.1680/geot.2007.00195.

Coop, M. R. (1990). The mechanics of uncemented carbonate sands. *Géotechnique* **40**, No. 4, 607–626, http://dx.doi.org/10.1680/geot.1990.40.4.607.

Delaunay, B. (1934). Sur la sphère vide. *Bulletin de l'Académie des Sciences de l'URSS, Classe des Sciences Mathématiques et Naturelles* **6**, 793–800 (in French).

Dong, C. & Wang, G. (2005). Curvatures estimation on triangular mesh. *J. Zhejiang Univ. Sci.* **6**, No. 1, 128–136.

Druckrey, A. M., Alshibli, K. A. & Al-Raoush, R. I. (2016). 3D characterization of sand particle-to-particle contact and morphology. *Comput. Geotech.* **74**, 26–35, https://doi.org/10.1016/j.compgeo.2015.12.014.

Fonseca, J. (2011). *The evolution of morphology and fabric of a sand during shearing*. PhD thesis, Imperial College London, London, UK.

Fonseca, J., O'Sullivan, C., Coop, M. & Lee, P. (2012). Non-invasive characterization of particle morphology of natural sands. *Soils Found.* **52**, No. 4, 712–722.

Fonseca, J., Bésuelle, P. & Viggiani, G. (2013). Micromechanisms of inelastic deformation in sandstones: an insight using x-ray micro-tomography. *Géotechnique Lett.* **3**, No. 2, 78–83.

Fonseca, J., Sim, W., Shire, T. & O'Sullivan, C. (2015a). Microstructural analysis of sands with varying degrees of internal stability. *Géotechnique* **64**, No. 5, 405–411, http://dx.doi.org/10.1680/geot.14.D.006.

Fonseca, J., Reyes-Aldasoro, C. C. & Wils, L. (2015b). Three-dimensional quantification of the morphology and intra-granular void ratio of a shelly carbonate sand. In *Deformation characteristics of geomaterials: proceedings of the 6th international symposium on deformation characteristics geomaterials* (eds V. A. Rinaldi, M. E. Zeballos and J. J. Clariá), pp. 551–558. Amsterdam, the Netherlands: IOS Press.

Fonseca, J., Nadimi, S., Reyes-Aldasoro, C. C., O'Sullivan, C. & Coop, M. R. (2016). Image-based investigation into the primary fabric of stress transmitting particles in sand. *Soils Found.* **56**, No. 5, 818–834.

Frossard, E. (1979). Effect of sand grain shape on interparticle friction; indirect measurements by Rowe's stress dilatancy theory. *Géotechnique* **29**, No. 3, 341–350, http://dx.doi.org/10.1680/geot.1979.29.3.341.

Golightly, C. R. (1989). *Engineering properties of carbonate sands*. PhD thesis, University of Bradford, Bradford, UK.

Gonzalez, R. C. & Woods, R. E. (2008). *Digital image processing*, 3rd edn. Upper Saddle River, NJ, USA: Prentice Hall, Inc.

Hawkins, A. E. (1993). *The shape of powder-particle outlines (Materials science & technology)*. Taunton, UK: Research Studies Press Ltd.

Henry, M., Pase, L., Ramos-Lopez, C. F., Lieschke, G. J., Stephen, A. R. & Reyes-Aldasoro, C. C. (2013). Phagosight: An open-source Matlab package for the analysis of fluorescent neutrophil and macrophage migration in a zebrafish model. *Plos One* **8**, No. 8, e72636.

Jardine, R., Chow, F., Overy, R. & Standing, J. (2005). *ICP design methods for driven piles in sands and clays*. London, UK: Thomas Telford Ltd.

Mathworks (2016). *MATLAB version 9.0 (R2016a)*. Natick, MA, USA: Mathworks, Inc.

Miao, G. & Airey, D. (2013). Breakage and ultimate states for a carbonate sand. *Géotechnique* **63**, No. 14, 1221–1229, http://dx.doi.org/10.1680/geot.12.P.111.

Nadimi, S. & Fonseca, J. (2017). On the tensile strength of soil grains in Hertzian response. *Proceedings of the 8th international conference on micromechanics of granular media, powders and grains*, Montpellier, France.

Otsu, N. (1979). A threshold selection method from gray level histograms. *IEEE Trans. Systems, Man, and Cybernetics* **9**, No. 1, 62–66.

Paniagua, P., Fonseca, J., Gylland, A. S. & Nordal, S. (2015). Microstructural study of deformation zones during cone penetration in silt at variable penetration rates. *Can. Geotech. J.* **52**, No. 12, 2088–2098.

Santamarina, J. C. & Cho, G. C. (2004). Soil behaviour: the role of particle shape. In *Advances in geotechnical engineering: the Skempton conference* (eds R. J. Jardine, D. M. Potts and K. G. Higgins), pp. 604–617. London, UK: ICE Publishing.

Semple, R. M. (1988). The mechanical properties of carbonate soils. In *Engineering for calcareous sediments* (eds R. J. Jewell and D. C. Andrews), pp. 807–836. Rotterdam, the Netherlands: Balkema.

Shi, Y. & Yan, W. M. (2015). Segmentation of irregular porous particles of various sizes from X-ray microfocus computer tomography images using a novel adaptive watershed approach. *Géotechnique Lett.* **5**, No. 4, 299–305.

Wählby, C., Sintorn, I. M., Erlandsson, F., Borgefors, G. & Bengtsson, E. (2004). Combining intensity, edge, and shape information for 2D and 3D segmentation of cell nuclei on tissue sections. *J. Microscopy* **215**, No. 1, 67–76.

Welzl, E. (1991). Smallest enclosing disks (balls and ellipsoids). *Lecture Notes Comput. Sci.* **555**, 359–370.

Wils, L., Van Impe, P. & Haegeman, W. (2015). One-dimensional compression of a crushable sand in dry and wet conditions. In *Geomechanics from micro to macro* (eds K. Soga, K. Kumar, G. Biscontin and M. Kuo), vol. 2, pp. 1403–1408. London, UK: Taylor and Francis Group.

Yan, W. M. & Shi, Y. (2014). Evolution of grain grading and characteristics in repeatedly reconstituted assemblages subject to one-dimensional compression. *Géotechnique Lett.* **4**, No. 3, 223–229.

Yasufuku, N. & Hyde, A. F. L. (1995). Pile end-bearing capacity in crushable sands. *Géotechnique* **45**, No. 4, 663–676, http://dx.doi.org/10.1680/geot.1995.45.4.663.

Zhang, X. & Baudet, B. A. (2013). Particle breakage in gap-graded soil. *Géotechnique Lett.* **3**, No. 2, 72–77.

Zhao, B. & Wang, J. (2016). 3D quantitative shape analysis on form, roundness, and compactness with μ-CT. *Powder Technol.* **291**, 262–275, https://doi.org/10.1016/j.powtec.2015.12.029.

Zuriguel, I., Mullin, T. & Rotter, J. M. (2007). Effect of particle shape on the stress dip under a sandpile. *Phys. Rev. Lett.* **98**, No. 2, 028001.